RSC Advances

PAPER

View Article Online
View Journal | View Issue

Cite this: *RSC Adv.*, 2023, **13**, 11591

Growth of carbon nanotubes over carbon nanofibers catalyzed by bimetallic alloy nanoparticles as a bifunctional electrode for Zn–air batteries†

Iram Aziz,[a] Xing Chen,[b] Xuhui Hu,[c] Wenjing (Angela) Zhang,*[d] Rabiya Javed Awan,[a] Ali Rauf[a] and Salman Noshear Arshad *[a]

Design of economical, large-scale, stable, and highly active bifunctional electrocatalysts for Zn–air batteries with enhanced oxygen reduction and oxygen evolution performance is needed. Herein, a series of electrocatalysts were facilely fabricated where *in situ* formed bimetallic nanoparticles aided in the growth of carbon nanotubes over carbon nanofibers (MM'-CNT@CNF) during thermal treatment. Different combinations of Fe, Ni, Co and Mn metals and melamine as precursor for CNT growth were investigated. The synergistic interaction between bimetallic nanoparticles and N-doped carbon results in greatly improved bifunctional catalytic activity for both oxygen reduction and evolution reactions (ORR, OER) using FeNi-CNT@CNF as catalyst. The half-wave potential (0.80 V *vs.* RHE) for FeNi-CNT@CNF for ORR was close to that of Pt/C (0.79 V *vs.* RHE), meanwhile its stability was superior to Pt/C. Likewise, during OER, the FeNi-CNT@CNF reached a current density of 10 mA cm^{-2} at a rather low overpotential of 310 mV *vs.* RHE compared to benchmark RuO_2 (410 mV). The rechargeable Zn-air prototype battery using FeNi-CNT@CNF as an air electrode outperformed the mixture of Pt/C and RuO_2 with discharge/charge overpotential of 0.61 V, power density of 118 mW cm^{-2} at 10 mA cm^{-2} and an improved cycling stability over 108 hours.

Received 17th January 2023
Accepted 22nd March 2023

DOI: 10.1039/d3ra00352c

rsc.li/rsc-advances

Introduction

Due to high-power density with zero carbon emissions, the Zn–air battery (ZAB) has emerged as a promising advanced energy conversion/storage technology.[1–3] However, the high overpotential required to carry out the oxygen evolution reaction (OER) and oxygen reduction reaction (ORR) at the air electrode returns an energy efficiency of 55–65% for rechargeable ZABs.[4] The commercially available benchmark IrO_2 and RuO_2 for OER[5] and Pt/C for ORR[6] are not practically scalable due to cost, scarce abundance of the metals, poor bifunctional activity, and stability issues.[7,8] One of the main challenges in the design of bifunctional electrocatalyst is that both OER and ORR require different active sites. Therefore, rational optimization of intrinsic active sites of suitable materials which can lead to improvement of surface characteristics such as enhanced increased surface area, accelerated mass and electron transport is vital to achieve high ORR/OER efficiency.[3]

In the past few years, numerous research studies revealed that non-precious transition metal (especially Fe, Co, Ni, Cr and Mn) and their derivatives (oxides, sulphides, nitrides, carbides, and mixed-metal alloys) based electrocatalysts have surpassed the OER/ORR activity of benchmark Pt/C and Ir/RuO_2 catalysts in alkaline medium.[9–16] Among all, alloying of two or more metals has gained much attention due to ease of tuning of electron energies and modification of surface properties in order to get perfect binding spots for the active species during the electrochemical process.[17] Furthermore, the use of a heteroatom (N, S, P, and B) doped carbonaceous matrix as support material for metal alloys provides extra stability to the resulting metal alloy/carbon composites, improves the conductivity, prevents agglomeration of metal nanoparticles, enhances active sites, and facilitates the adsorption/desorption of the O_2.[18,19] In this regard, a series of non-precious bimetallic alloys supported over a heteroatom doped carbon matrix *e.g.* CoFe@NC,[20] CuCo@NC,[21,22] CoFe@PC,[23] NiCo@$NiCoO_2$/C,[24] NPCN/CoNi-NCNT,[25] $MnCo_2O_4$@C,[26] and FeNi/N-CPCF[27] have

[a]*Department of Chemistry and Chemical Engineering, Syed Babar Ali School of Science and Engineering, Lahore University of Management Sciences, Lahore 54792, Pakistan. E-mail: salman.arshad@lums.edu.pk*

[b]*School of Mechanical Engineering, Northwestern Polytechnical University, Xi'an, 710072, P. R China*

[c]*College of Chemistry and Molecular Sciences, Wuhan University, Wuhan 430072, Hubei, People's Republic of China*

[d]*Department of Environmental Engineering, Technical University of Denmark, DTU, 2800 Kgs. Lyngby, Denmark. E-mail: wenz@env.dtu.dk*

† Electronic supplementary information (ESI) available: SEM images and XPS data. See DOI: https://doi.org/10.1039/d3ra00352c

been successfully fabricated, exhibiting superior OER/ORR performance. Despite the progress made to develop efficient bifunctional electrocatalysts, the less than satisfactory activity, stability issues and lack of insight into the nature of active sites for OER/ORR is still driving scientists and engineers towards the development of novel electrocatalysts with better performance at low cost.[28]

In order to design a highly efficient bifunctional electrocatalyst, several facile strategies have been employed such as (i) nano-structuring of transition metals to increase activity and selectivity of catalytic sites,[29] (ii) constructing nanohybrids of transition metals alloys anchored with various allotropes of carbon such as graphene and CNTs which resulted in enhancement of conductivity and surface area, reduces the agglomeration of active species, and the synergistic effect from carbon support and active sites improves the overall catalytic activity,[30,31] and (iii) heteroatom doping in carbon to modify the electronic structure for tunable catalytic activity.[21,24,27] To combine all these strategies, a facile and cost-effective synthetic protocol is desired. Besides, the effect of different bimetallic alloy nanoparticle towards the growth of carbon nanostructures and the respective bifunctional electrochemical performance of resulting nanocomposites is an interesting research area to explore.

Here, we have reported a relatively facile and potentially scalable method to fabricate bifunctional electrocatalysts where carbon nanotubes are grown and anchored over carbon nanofibers using bimetallic alloy nanoparticles (MM′-CNT@CNF). These showed excellent activity for both ORR and OER processes when used as air electrode for ZAB. The method involved electrospinning a blend solution of polyacrylonitrile, polyvinylpyrrolidone, melamine, and metal (Fe/Co/Mn/Ni) salts to prepare precursor nanofibers. Pyrolyzing these under inert argon environment triggered the growth of carbon nanotubes anchored over carbon nanofibers with bimetallic nanoparticles encapsulated at CNT tips. Among all combinations made, the FeNi-CNT@CNF nanocomposite exhibited superior OER and ORR performance and outperformed Pt/C + RuO_2 counterparts when tested as air electrode in ZAB. This work also provides a useful comparison of variation in structure of CNTs grown using different bimetallic metal alloys as catalyst and their respective electrochemical performance as OER/ORR catalyst.

Experimental

Fabrication of bimetallic alloys catalyzed CNT@CNFs

First, the electrospinning blend solution was prepared by overnight stirring of 900 mg of PAN and 1 g of PVP in 10 mL of DMF. The nanofibers were prepared by electrospinning of this solution at 20 kV with 20 cm distance between needle and collector. After stabilizing the NFs at 250 °C for 2 h in air, they were impregnated overnight in ethanol solution of 0.5 M $FeCl_3$, 0.25 M $NiCl_2$, 0.25 M $MnCl_2$ and 0.25 M $CoCl_2$. After that, 3 g of melamine was added and stirred for 5 min and left for 12 h at room temperature. After collecting nanofibers by rotary evaporator they were dried in a heating oven. Lastly, these were carbonized in an Ar controlled tube furnace by heating at 800 °C for 2 h using a heating rate of 4 °C min^{-1}.[32] The samples are labelled as FeNi-CNT@CNF, FeCo-CNT@CNF, FeMn-CNT@CNF, NiCo-CNT@CNF, NiMn-CNT@CNF, CoMn-CNT@CNF, Fe-CNT@CNF, Ni-CNT@CNF, and Co-CNT@CNF. No CNT growth was observed for Mn-CNT@CNF (Fig. S1†), thus, it was not investigated further in this study.

Material characterization

Structural characterization was done by collecting Powder X-ray diffraction (PXRD) data in the scan range of 0–70° 2θ using Rigaku XRD-6000 (Cu Kα, 40 kV, 30 mA). Thermo Scientific™ Nexsa™ X-ray Photoelectron Spectrometer (XPS) was performed for binding energy analysis and to estimate the nitrogen content. The sizes, morphologies, and elemental analysis of the fabricated catalysts were studied by scanning electron microscopy (SEM) using QFEG 200 Cryo ESEM equipped with energy-dispersive X-ray spectroscopy (EDX). Detailed structural investigation was done by transmission electron microscopy (TEM) analysis with Titan Analytical 80–300 ST TEM. Inductively Coupled Plasma Optical Emission Spectroscopy (ICP-OES) was used to calculate the metallic content in the prepared MM′-CNT@CNF.

Electrochemical characterization

The electrochemical characterizations were done on BioLogic SP-300 potentiostat. The ORR measurements were carried out using a three-electrode system with the working electrode of glassy carbon (GC, with ring area 0.196 mm^2) rotating ring disk (RDE), reference electrode of Ag/AgCl, and counter electrode of graphite rod. The catalyst ink, supported on the working electrode, was prepared by finely grinding 5 mg of the sample and ultrasonically dispersing it in 1 mL of DMF and 10 μl of Nafion solution. 5 μl of this slurry was drop casted on the working electrode and dried in air giving a mass loading of 0.200 mg cm^{-2}. O_2 (or Ar) was bubbled through the electrolyte (0.1 M KOH) for 30 min to saturate it. The working electrode was cycled 50 times (scan rate 50 mV s^{-1}) under Ar gas purging before recording the cyclic voltammogram (CV) in O_2 saturated electrolyte (scan rate 10 mV s^{-1}). Linear sweep voltammetry (LSV) RDE in the range 400–2400 rpm was performed. Chronoamperometric measurements were performed at 0.7 V and 1600 rpm *vs.* reversible hydrogen electrode (RHE) under continuous purging of O_2. Similarly, for OER measurements, working electrode of GC with disc area 0196 mm^2, reference electrode of Hg/HgO, and counter electrode of Pt were used.

Koutecky–Levich (K–L) plots using the below equations were used to estimate the electron transfer numbers.

$$\frac{1}{j} = \frac{1}{B\omega^{0.5}} + \frac{1}{j_k}$$

$$B = 0.2nF(D_{O_2})^{2/3}v^{-1/6}C_{O_2}$$

where j is the measured electron current density, j_k is the kinetic current density, ω is the rpm of the working electrode, F is the Faraday constant (96 485 C mol^{-1}), C_{O_2} is O_2 bulk concentration

(1.2×10^{-6} mol cm^{-1}); D_{O_2} is the O_2 diffusion coefficient (1.9×10^{-5} cm^2 s^{-1}), ν is the kinetic viscosity of the electrolyte (0.01 cm^2 s^{-1}), and n is the electron transfer number.

The double layer capacitance C_{dl} was calculated by CV measurements at various scan rates in the range 2–10 mV s^{-1}. Anodic (j_a) and cathode (j_c) current densities were recorded and plotted as (j_a–j_c) at 1.12 V *vs.* RHE. The specific capacitance C_s was 0.04 mF cm^{-2} in the non-faradaic region. C_{dl}/C_s value gives the electrochemically active surface area (ECSA).

Zn–air battery testing

FeNi-CNT@CNF and 1 : 1 mixture of 20% Pt/C + RuO_2 were assembled into a custom-made ZAB testing setup using polished Zn foil as anode and mixed solution of 6 M KOH and 0.2 M zinc acetate as electrolyte. The prepared catalysts or mixed commercial Pt/C and RuO_2 in 1 : 1 mass ratio was coated on the carbon paper and used as the air cathode. The galvanostatic charge and discharge were performed, using BioLogic battery testing station system (SP-300), by a recurrent galvanostatic pulse method at 10 mA cm^{-2} current density. A 10 min discharge and 10 min charge cycles were used under ambient conditions.

Results and discussion

Morphology and structural characterization

As illustrated in Fig. 1, PAN/PVP precursor solution was used to fabricate electrospun PAN/PVP nanofibers (NFs). After stabilizing at 250 °C for 2 hours, the pre-oxidized PAN/PVP NFs were submerged in alcoholic solution of metal salt and melamine. Herein, melamine is used as precursor for fabrication of CNTs due to its N atom rich nature and metal salts as precursor for the growth of metal alloy NPs. After the complete removal of ethanol from the solution, the dried NFs coated with metal ions and melamine were pyrolyzed at 800 °C, which resulted into formation of FeNi-CNT@CNF nanocomposites.

SEM was performed to observe the morphology of the prepared electrocatalysts as presented in Fig. 2 and S2, S3, and S4.† All samples illustrate the formation of 3D hierarchical CNT@CNF structure with metal alloy NPs present at the tip of CNT and some of the metal NPs also observed to be embedded in CNFs. The size, shape, and density of CNTs on CNFs surface varies by changing the metal combination, signifies that type of metal alloy/metal dictate the morphology and density of CNTs on CNFs surface. SEM analysis further reveals that a major portion of CNTs are bamboo-shaped which confirms the N atom doping in graphitic carbon structure.[33] From the TEM analysis of FeNi-CNT@CNF in Fig. 2d, we can further confirm that CNTs fabricated using melamine as precursor are bamboo-shaped with FeNi NPs encapsulated in CNTs. HR-TEM in Fig. 2e showed that well crystallized FeNi NPs are embedded in onion shaped graphitic layers with general thickness of ~2–5 nm. Interfacial analysis of FeNi and carbon layers in Fig. 2f reveals 0.21 nm interplanar distance of face centered cubic (FCC) FeNi NP which corresponds to (111) plane. The 0.37 nm interplanar distance of the outer graphitic layer can be indexed to (002) plane of the graphitic carbon. The energy dispersive X-ray spectroscopy (EDX) analysis in SEM mode (Fig. 2g) further confirms the presence of C, Fe, and Ni elements in FeNi-CNT@CNF. The average diameter of CNT was calculated for FeNi-CNT@CNF and found to be 32.93 ± 13.02 nm (Fig. 2h).

The average CNT diameter distribution was also measured and represented in Fig. S2, S3, and S4† for rest of the samples. The observed inconsistency in diameter of the obtained CNTs can be attributed to the different binary metal combinations used as catalysts. The catalytic efficiency of mono-metals for nucleation and growth of CNTs varies from metal to metal. For example, Ni is more active than Co for initiating nucleation, whereas Co is more efficient for catalyzing the growth of CNTs. The pros can be synergistically combined by using bimetallic alloy nanoparticles *e.g.*, it can result in a significantly enlarged tube size for MM′-CNT@CNF.[34] Moreover, the CNT size depends

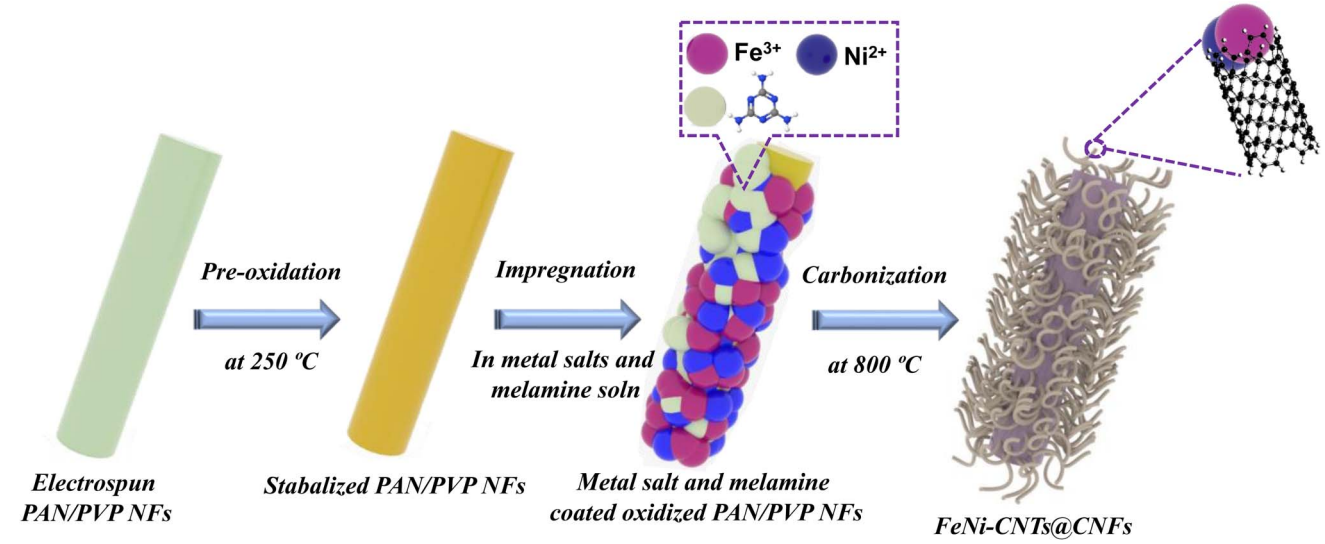

Fig. 1 Schematic illustration for synthesis of FeNi-CNT@CNF nanocomposite.

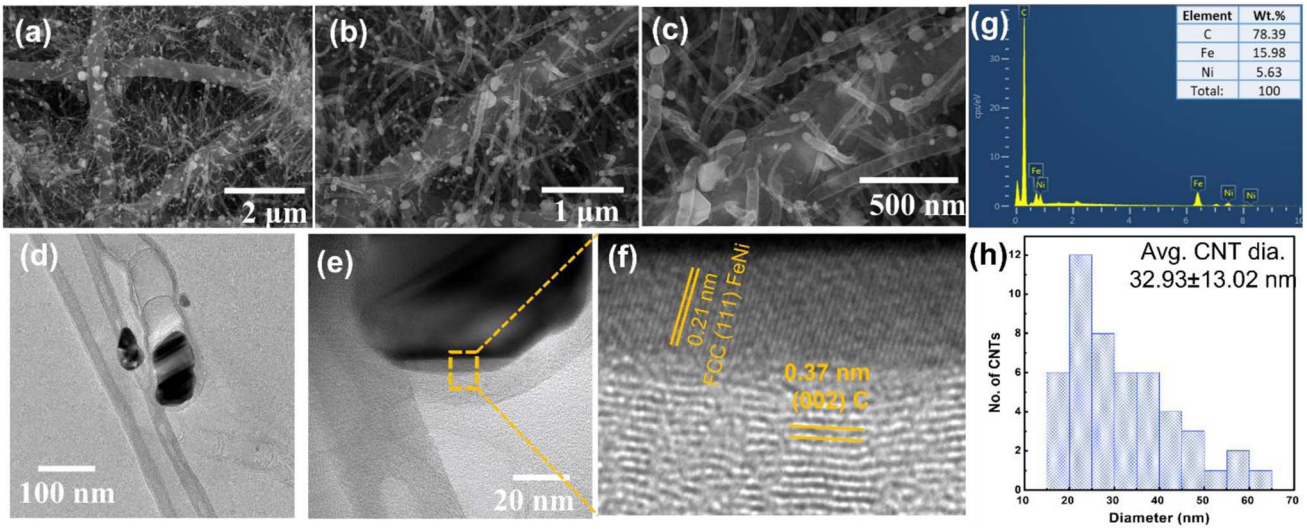

Fig. 2 (a–c) SEM images of FeNi-CNT@CNF at different magnifications, (d) TEM image of bamboo-shaped CNTs with FeNi nanoparticles encapsulated at CNTs tip, (e) FeNi NP encapsulated with thick graphene layers, (f) interface between FeNi NP and graphene layers, (g) EDX map of FeNi-CNT@CNF, and (h) CNT diameter distribution for FeNi-CNT@CNF.

on the combination of metals. For example, FeMn-CNT@CNF has a very large CNT diameter (≈155 nm), whereas FeNi-CNT@CNF (≈32.0 nm), NiMn-CNT@CNF (≈37.9 nm), CoMn-CNT@CNF (≈29.10 nm), NiCo-CNT@CNF (≈32.81 nm), and FeCo-CNT@CNF (≈17.24 nm) have thinner CNTs (Fig. S3 and S4†). A large CNT diameter is considered favorable for mass transfer by providing larger spaces for transportation of ions and other species.[35] The durable and continuous CNT structure for MM′-CNT@CNF is anticipated to facilitate charge transport and improve ion exchangeability. Fe-CNT@CNF sample has short and small diameter CNTs (≈22.81 nm) compared with the thicker CNTs (≈30.32 nm) for Ni-CNT@CNF and Co-CNT@CNF (≈45.37 nm). Furthermore, previous studies revealed that the formation of bimetallic alloys also assist in regulating the grain size.[36] The growth of crystallites is restricted by heterogeneous nucleation of grain boundaries,[37] leading to higher active sites density for enhanced catalytic activity.[38,39]

The crystalline phases for all the samples were investigated by XRD and presented in Fig. 3 with (002) plane of carbon at $2\theta \approx 26°$ being common to all the samples. FeNi-CNT@CNF, FeCo-CNT@CNF, NiCo-CNT@CNF, Fe-CNT@CNF, Ni-CNT@CNF, and Co-CNT@CNF exhibited FCC crystal structure with diffraction peaks at ≈44° for (111), 51° for (200), and 76° for (220) planes ($Pm\bar{3}m$, ICOD 01-088-1715). For rest of the samples FeMn-CNT@CNF, NiMn-CNT@CNF, and CoMn-CNT@CNF, in addition to diffraction peaks corresponding to FCC planes, cubic MnO peaks also appeared at ≈36°, 43°, and 59° corresponding to (110), (200), and (211) planes ($Fm\bar{3}m$, ICOD 01-078-0424).

The chemical composition and states of FeNi-CNT@CNF and rest of the prepared catalysts were investigated by XPS, as presented in Fig. 4. High resolution XPS spectrum of Fe 2p (Fig. 4a), presented broadened Fe $2p_{3/2}$ and Fe $2p_{1/2}$ peaks centered around 712.4 and 723.6 eV, respectively. A satellite peak of Fe^{3+} is present at 718.4 eV.[40] In the Ni 2p spectrum (Fig. 4b), the Ni $2p_{3/2}$ (Ni^{2+}) and Ni $2p_{1/2}$ (Ni^{2+}) peaks are present at 855.2 and 872.9 eV, respectively, along with the appearance of shakeup satellite peak at 862.4 eV.[41] There are no metallic Fe and Ni are detected in the XPS spectra, which could be due to the surface oxidation of FeNi alloy.[42] The deconvolution of N 1s (Fig. 4c) represent the presence of pyridinic N, M – N, pyrrolic N, graphitic N, and pyridinic N-oxide located at 398.5, 401.2, 402.5, 405.4, and 406.1 eV, respectively.[43] The O 1s spectrum was deconvoluted (Fig. 4d) into four components at 529.6, 532.3, and 535.2 eV, which are assigned to the lattice oxygen M–O, C=O, and C–O bonding, respectively.[44]

Formation of strong interaction between carbon and metal nanoparticles are important in improving the overall catalytic activity and stability and can be observed in N 1s spectrum (Fig. S5†). Proportions of different nitrogen doped in resulting

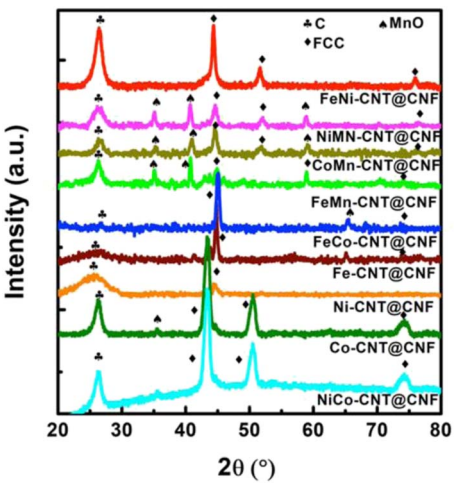

Fig. 3 XRD comparison of FeNi, MnCo, NiCo, NiMn, FeMn, FeCo, Co, Ni, and Fe NPs containing CNT@CNF nanocomposites.

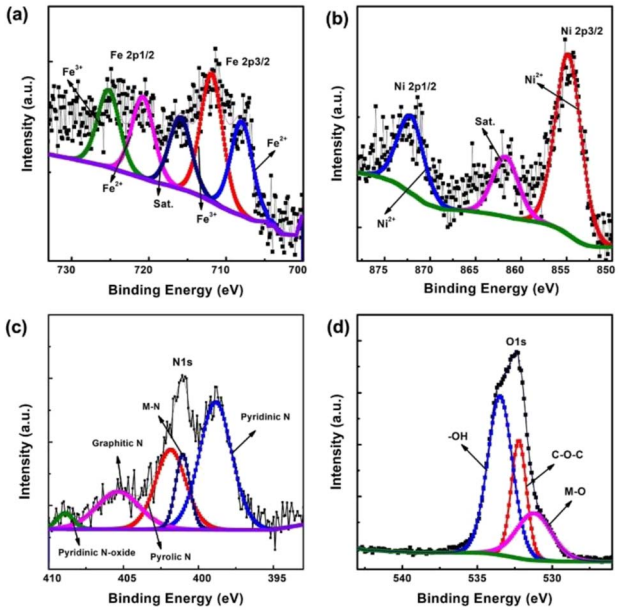

Fig. 4 XPS spectra of (a) Fe 2p, (b) Ni 2p, (c) N 1s, and (d) O 1s of FeNi-CNT@CNF.

nanostructures are also calculated in Table S1,† the results revealed that bimetallic addition leads to increased amount of pyridinic-N and M-N. Pyridinic-N is widely considered important for ORR reactions as it improves the coordination between transition metal and N-doped carbon. The improved coupling interaction lowers the contact resistance and favored the charge transport. Furthermore, the presence of graphitic-N in both MM′-CNT@CNF and M-CNT@CNF reflects higher degree of graphitization which improves the electrical conductivity due to the electronegativity difference between C and N.[45,46]

The Bruner–Emmette–Teller surface area S_{BET} was also calculated using nitrogen adsorption–desorption isotherm as represented in Fig. S6 and Table S2.† There is a significant increase in the surface area for FeNi nanoparticle containing CNT@CNF (S_{BET} = 60.275 m^2 g^{-1}) as compared to Fe-CNT@CNF (S_{BET} = 6.340 m^2 g^{-1}) and Ni-CNT@CNF (S_{BET} = 21.610 m^2 g^{-1}). The increase in the lengths of CNT in FeNi-CNT@CNF could be one of the reasons for increase in the specific surface area which exposes higher number of active sites for improved bifunctional catalytic activity.

Electrochemical measurements

ORR activity

ORR activity of the materials was first characterized using CV in O_2 and Ar saturated 0.1 M aqueous KOH electrolyte (Fig. 5a). Compared with Ni-CNT@CNF and Fe-CNT@CNF, FeNi-

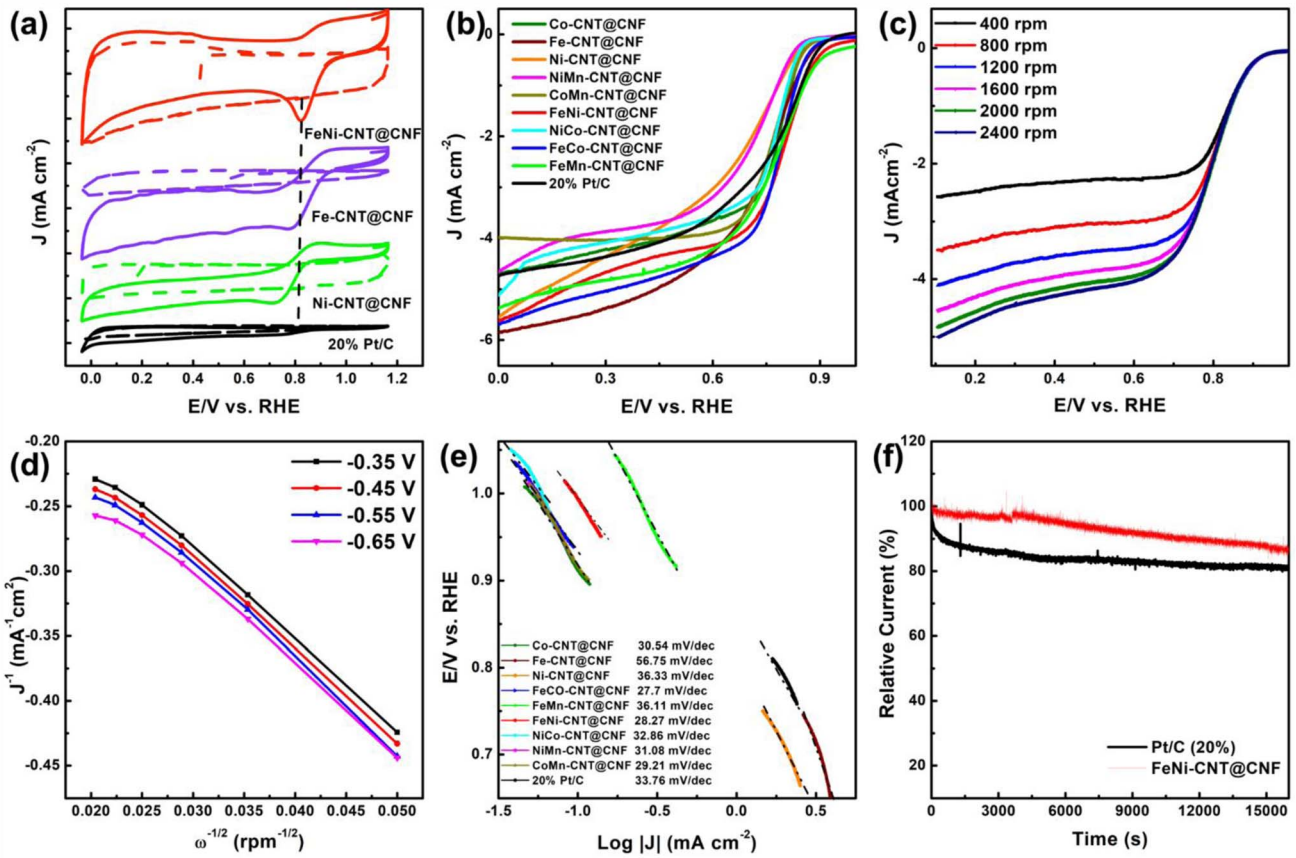

Fig. 5 (a) CV plots in O_2 (solid line) and Ar (dashed line) saturated 0.1 M KOH, (b) LSV polarization curves in O_2 saturated 0.1 M KOH, (c) LSV of NiFe-CNT@CNF at different rotating speeds, (d) corresponding K–L plot, (e) Tafel plots, and (f) stability plots for FeNi-CNT@CNF and 20% Pt/C.

CNT@CNF shows a more positive oxidation peak (0.81 V *vs.* RHE) and a relatively larger cathodic peak current density which exceeds that of Pt/C (oxidation peak potential is 0.79 V *vs.* RHE).

Linear sweep voltammetry (LSV) results in Fig. 5b further compares the ORR activity. The mono-metal based catalysts (Fe-CNT@CNF, Ni-CNT@CNT, and Co-CNT@CNF) exhibited a more negative onset potential with a lower current density than MM′-CNT@CNF. Moreover, the ORR activities of FeNi-CNT@CNF are similar to benchmark 20% Pt/C as shown by E_{onset} and $E_{1/2}$ values (Fig. 5c). In addition, compared with Ni-CNT@CNF (0.64 V) and Fe–N/C (0.76 V), the $E_{1/2}$ of FeNi-CNT@CNF (0.80 V) is much higher. The outstanding ORR activity of FeNi-CNT@CNF can be credited to the improved active sites on bimetallic NPs and increased proportion of Pridinic N and M – N in carbon nanostructures which facilitates efficient ORR catalysis.

For maximum ORR efficiency, a 4e− pathway is highly desired. RDE voltammograms at 400–2400 rpm rotating speeds is useful to understand the kinetics and 4e− selectivity. Expectedly, faster rotating speeds enhances the limiting current density due to availability of more O_2 on the electrode surface (Fig. 5c). The electron transfer number (n) for FeNi-CNT@CNF is estimated to be ≈4 using slopes of Koutecky–Levich (K–L) plots implying high 4e− selectivity of FeNi-CNT@CNF for oxygen reduction. The Tafel slopes were also calculated to evaluate the catalytic kinetics for ORR. Compared to 20% Pt/C (33.76 mV dec^{-1}), Ni-CNT@CNF (36.33 mV dec^{-1}), Co-CNT@CNF (30.54 mV dec^{-1}), Fe-CNT@CNF (56.75 mV dec^{-1}), NiMn-CNT@CNF (31.08 mV dec^{-1}), FeMn-CNT@CNF (36.11 mV dec^{-1}), NiCo-CNT@CNF (32.86 mV dec^{-1}), CoMn-CNT@CNF (29.21 mV dec^{-1}); FeCo-CNT@CNF and FeNi-CNT@CNF have a lower Tafel slope of 27.7 mV dec^{-1} and 28.27 mV dec^{-1}, respectively. The lower Tafel slope values for FeNi-CNT@CNF compared to Fe-CNT@CNF and Ni-CNT@CNF further signify that formation of bimetallic alloy improves the catalytic active sites on the heterostructure and facilitate charge transport efficiently.

Next, the stability of FeNi-CNT@CNF and 20% Pt/C were also measured and compared at −0.7 V *vs.* RHE in O_2 saturated 0.1 M KOH at 1600 RPM. As presented in Fig. 5f, after 15 000 s, FeNi-CNT@CNF retained 85% of its original activity while the 20% Pt/C catalyst was degraded more with only 79% retention under similar testing conditions. The outstanding robustness of FeNi-CNT@CNF can be credited to its robust carbon-based hierarchical structure and the encapsulation of FeNi active sites by a few graphene layers. Overall, above results demonstrate that the FeNi-CNT@CNF with greater active sites can function well in ORR because of enhanced oxygen adsorption,

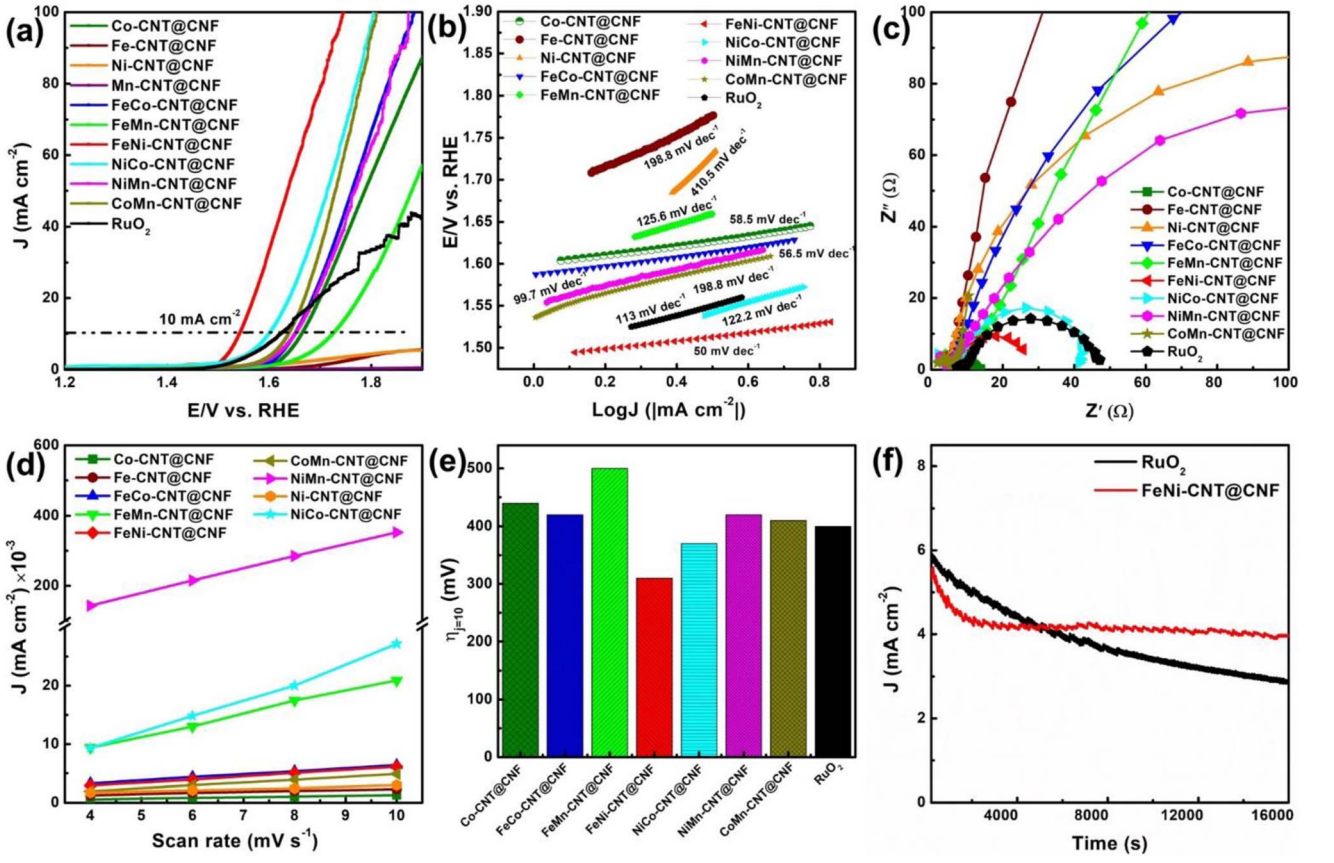

Fig. 6 (a) LSV polarization curves of prepared catalysts and RuO_2, (b) the corresponding Tafel slopes, (c) EIS plots, (d) C_{dl}, (e) comparison of overpotential for the prepared electrocatalysts and RuO_2 at $J = 10$ mA cm^{-2}, and (f) OER chronoamperometric response of FeNi-CNT@CNF and RuO_2 at a constant potential of 1.56 V (*vs.* RHE).

ion-diffusion, and electron-transfer. The Fe and Ni content of the FeNi-CNT@CNF nanocomposite was measured by ICP-OES and found to be 18.8 wt% Fe and 9.3 wt% Ni. These results are consistent with our initial molar ratios of salts used *i.e.* 0.5 M $FeCl_3$ and 0.25 M $NiCl_2$. The nitrogen content was calculated by XPS and found to be 2.4 wt%. The C content is then estimated by balance of these *i.e.* 69.5 wt%.

OER activity

Electrocatalytic activity for OER was investigated in 1 M KOH. The LSV polarization curves in the Fig. 6a shows that FeNi-CNT@CNF catalyst exhibit distinctly improved catalytic activity compared to the rest of the MM′-CNT@CNF, M-CNT@CNF, and benchmark RuO_2, with an onset potential (E_{onset}) of 1.48 V. E_{onset} is defined as the potential required to attain OER current density of 0.2 mA cm^{-2}. Moreover, the FeNi-CNT@CNF presented a low overpotential of ~310 mV at 10 mA cm^{-2} (Fig. 6e), which is much lower to that of the noble metal (RuO_2) catalysts (~400 mV). The lower overpotential of FeNi-CNT@CNF as compared to prepared electrocatalysts and commercial RuO_2 can be ascribed to the superior catalytic activity of FeNi NP present at the tips of CNTs and enhanced gas diffusion and mass transfer facilitated due to CNT@CNF 3D free standing hierarchical structure. Subsequently, the catalytic kinetics of prepared electrocatalysts and commercial RuO_2 is assessed by the Tafel plots. As displayed in Fig. 6b, the resultant Tafel slope of FeNi-CNT@CNF (50 mV dec^{-1}) is much smaller than rest of the electrocatalysts and the commercial RuO_2 (113 mV dec^{-1}) implying superior kinetics. Electrochemical impedance spectra (EIS) (Fig. 6c) indicate that FeNi-CNT@CNF has a much lower impedance and thus a higher charge-transfer rate and evidently faster OER kinetics than the rest of the electrocatalysts. The electrochemical double layer capacitance (C_{dl}) was employed to investigate the electrochemical active surface area. However, the highest calculated C_{dl} of 34.863 mF cm^{-2} is obtained for NiMn-CNT@CNF, which is much higher than that of NiCo-CNT@CNF (2.935 mF cm^{-2}), FeMn-CNT@CNF (1.949 mF cm^{-2}), FeNi-CNT@CNF (0.537 mF cm^{-2}), FeCo-CNT@CNF (0.5165 mF cm^{-2}), CoMn-CNT@CNF (0.488 mF cm^{-2}), Ni-CNT@CNF (0.208 mF cm^{-2}), Fe-CNT@CNF (0.172 mF cm^{-2}) and Co-CNT@CNF (0.123 mF cm^{-2}). Comparatively, the ECSA at same mass loading of MM′-CNT@CNF outperform those of M-CNT@CNF which can be ascribed to the increased pyridinic-N content, lengthier and robust CNTs, and smaller metal particle size. However, it can be

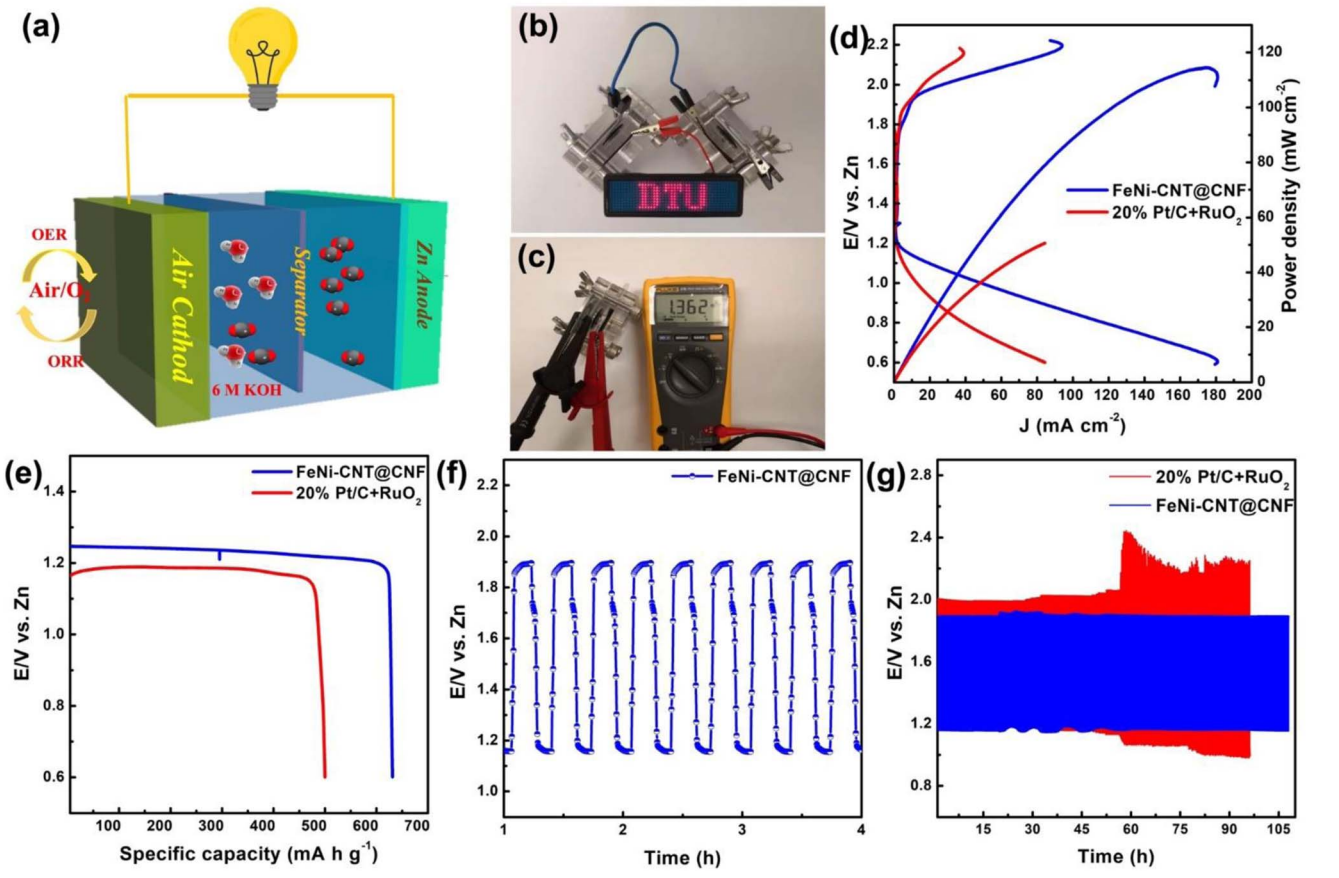

Fig. 7 (a) Schematic illustration of the ZAB, (b) photograph of a LED (~3.0 V) powered by two ZAB in series using FeNi-CNT@CNF air cathode, (c) open-circuit potential of FeNi-CNT@CNF air electrode containing ZAB, (d) galvanodynamic discharge profiles and power density curves of FeNi-CNT@CNF and 20% Pt/C + RuO_2 catalyzed cathode, (e) specific capacity profiles of ZABs at the current density of 10 mA cm^{-2}, (f & g) discharge/charge cycling curves at current density of 10 mA cm^{-2} of ZAB and 20% Pt/C + RuO_2.

observed that, for MM′-CNT@CNF, the ECSA doesn't necessarily correlate with their catalytic activity. For instance, FeNi-CNT@CNF attains the best ORR and OER catalytic performance, while NiMn-CNT@CNF, which has a much lower catalytic activity to FeNi-CNT@CNF, has largest C_{dl} value. The defect concentration of CNTs and interaction between metal and carbon affect the electronic conductivity and charge transfer resistance which enhances the current density, but these effects cannot be easily decoupled and quantified.[47] Much higher value of C_{dl} for NiMn-CNT@CNF can be attributed to the large diameter and high density of CNTs on the surface of CNFs (Fig. S4a–d†). The excellent stability of the FeNi-CNT@CNF (Fig. 6f) is evident by a minor deterioration of anodic current after 16 000 s at 1.56 V potential. The superior stability compared to commercial RuO_2, is mainly due to the 3D hierarchical structure of the FeNi-CNT@CNF. The morphological analysis of the cycled catalyst was done by SEM and the images in Fig. S7† reveals good structural stability.

Zn–air battery testing

The superior bifunctional catalytic activity of FeNi-CNT@CNF for ORR and OER motivated the testing of FeNi-CNT@CNF in rechargeable ZAB. Zinc foil as anode and carbon cloth loaded with the catalyst as air cathode was used for Zn-battery testing in 6 M KOH as electrolyte (Fig. 7a). 20% Pt/C and RuO_2 (1 : 1 mass ratio) were also tested as air cathode under similar test conditions. As shown in Fig. 7c, the open circuit voltage of ZAB was maintained at 1.362 V compared to 1.30 V for 20% Pt/C + RuO_2. The charge–discharge profiles in Fig. 7d demonstrates that the FeNi-CNT@CNF based battery showed a higher discharge voltage of 0.99 V compared to 0.75 V for 20% Pt/C + RuO_2 at 100 mA cm^{-2} and this observation was consistent at different current densities. The maximum power density of FeNi-CNT@CNF based battery is 118 mW cm^{-2} compared to only 50 mWcm^{-2} for 20% Pt/C + RuO_2. Moreover, FeNi-CNT@CNF exhibited a lower discharge/charge overpotential of 0.8 V compared to 1.04 V for Pt/C. Also, the FeNi-CNT@CNF based ZAB consumes Zn more efficiently as shown by the specific capacity of 650 mA h g^{-1} which is greater than that of 20% Pt/C + RuO_2 (500 mA h g^{-1}). With charge–discharge cycles at 5 mA cm^{-2} for 108 h, the ZAB using the FeNi-CNT@CNF shows charge/discharge voltage gap of ~0.65 V which is lower than Pt/C catalyst (~0.9 V).

Conclusion

In this work, bimetallic nanoparticles addition to N-doped CNT@CNF is shown to enhance the bifunctional oxygen electrocatalysis. These catalysts are synthesized by heat treatment of precursor nanofibers of PAN/PVP containing metal/bimetallic nanoparticles and melamine which drives the growth of CNTs. This synthesis approach resulted in increased pyridinic-N and M – N content, longer and robust CNTs, and stronger coupling between bimetal and carbon support resulting in enhanced activity and durability. The FeNi-CNT@CNF demonstrated enhanced ORR activity with $E_{1/2}$ of 0.80 V and OER activity with an overpotential of 310 mV at 10 mA cm^{-2}. Moreover, they were durable and superior to benchmark catalysts tested under similar conditions. When used as the air cathode of a rechargeable ZAB, the FeNi-CNT@CNF-based battery showed a larger open-circuit voltage of 1.362 V and larger power density (118 mW cm^{-2}) compared with the Pt/C + RuO_2-based battery. This work highlights the importance of rationally designing new carbon-based material systems to support bifunctional oxygen electrolysis which can be economically scaled up.

Author contributions

Iram Aziz: investigation, formal analysis, methodology, project administration, writing original draft; Xing Chen & Xuhui Hu: investigation, methodology; Wenjing (Angela) Zhang: supervision, resources; Ali Rauf: review; Rabiya Javed Awan: investigation; Salman Noshear Arshad: conceptualization, resources, project administration, supervision, writing review and editing.

Conflicts of interest

There are no conflicts of interest to declare.

Acknowledgements

Funding from Higher Education Commission (HEC) of Pakistan under NRPU program (grant numbers 4430 and 5911) is greatly acknowledged to carry out this research. Funding for Ms Iram Aziz, lead author, to carry out research at DTU was provided by Higher Education Commission (HEC) under International Research Support Initiative Program (IRSIP) and at LUMS under Indigenous PhD Fellowship Program.

Notes and references

1 J. Fu, Z. P. Cano, M. G. Park, A. Yu, M. Fowler and Z. Chen, *Adv. Mater.*, 2017, **29**(7), 1604685.
2 P. Tan, B. Chen, H. Xu, H. Zhang, W. Cai, M. Ni, M. Liu and Z. Shao, *Energy Environ. Sci.*, 2017, **10**, 2056–2080.
3 H. F. Wang, C. Tang and Q. Zhang, *Adv. Funct. Mater.*, 2018, **28**, 1–22.
4 E. Davari and D. G. Ivey, *Sustainable Energy Fuels*, 2018, **2**, 39–67.
5 Y. Lee, J. Suntivich, K. J. May, E. E. Perry and Y. Shao-Horn, *J. Phys. Chem. Lett.*, 2012, **3**, 399–404.
6 U. A. Paulus, T. J. Schmidt, H. A. Gasteiger and R. J. Behm, *J. Electroanal. Chem.*, 2001, **495**, 134–145.
7 Y. Zhu, W. Zhou and Z. Shao, *Small*, 2017, **13**, 1–25.
8 M. Kuang and G. Zheng, *Small*, 2016, **12**, 5656–5675.
9 Y. Zhao, K. Kamiya, K. Hashimoto and S. Nakanishi, *J. Phys. Chem. C*, 2015, **119**, 2583–2588.
10 M. Yan, K. Mao, P. Cui, C. Chen, J. Zhao, X. Wang, L. Yang, H. Yang, Q. Wu and Z. Hu, *Nano Res.*, 2020, **13**, 328–334.
11 H. Zhu, J. Zhang, R. Yanzhang, M. Du, Q. Wang, G. Gao, J. Wu, G. Wu, M. Zhang, B. Liu, J. Yao and X. Zhang, *Adv. Mater.*, 2015, **27**, 4752–4759.

12 Z. S. Wu, S. Yang, Y. Sun, K. Parvez, X. Feng and K. Müllen, *J. Am. Chem. Soc.*, 2012, **134**, 9082–9085.
13 W. Yan, Z. Yang, W. Bian and R. Yang, *Carbon*, 2015, **92**, 74–83.
14 X. Hu, F. Cheng, N. Zhang, X. Han and J. Chen, *Small*, 2015, **11**, 5545–5550.
15 P. W. Menezes, A. Indra, D. González-Flores, N. R. Sahraie, I. Zaharieva, M. Schwarze, P. Strasser, H. Dau and M. Driess, *ACS Catal.*, 2015, **5**, 2017–2027.
16 H. Y. Wang, Y. Y. Hsu, R. Chen, T. S. Chan, H. M. Chen and B. Liu, *Adv. Energy Mater.*, 2015, **5**, 1–8.
17 V. R. Stamenkovic, B. S. Mun, M. Arenz, K. J. J. Mayrhofer, C. A. Lucas, G. Wang, P. N. Ross and N. M. Markovic, *Nat. Mater.*, 2007, **6**, 241–247.
18 Y. J. Wang, H. Fan, A. Ignaszak, L. Zhang, S. Shao, D. P. Wilkinson and J. Zhang, *Chem. Eng. J.*, 2018, **348**, 416–437.
19 C. Zhu, Y. Aoki and H. Habazaki, *Part. Part. Syst. Charact.*, 2017, **34**, 1–12.
20 Y. Xiong, Y. Yang, F. J. Disalvo and H. D. Abruña, *J. Am. Chem. Soc.*, 2019, **141**, 10744–10750.
21 M. Kuang, Q. Wang, P. Han and G. Zheng, *Adv. Energy Mater.*, 2017, **7**, 1–8.
22 M. Huo, B. Wang, C. Zhang, S. Ding, H. Yuan, Z. Liang, J. Qi, M. Chen, Y. Xu, W. Zhang, H. Zheng and R. Cao, *Chem. – Eur. J.*, 2019, **25**, 12780–12788.
23 Z. Lionet, S. Nishijima, T. H. Kim, Y. Horiuchi, S. W. Lee and M. Matsuoka, *Dalton Trans.*, 2019, **48**, 13953–13959.
24 H. Xu, Z. X. Shi, Y. X. Tong and G. R. Li, *Adv. Mater.*, 2018, **30**, 1–8.
25 Y. Hou, S. Cui, Z. Wen, X. Guo, X. Feng and J. Chen, *Small*, 2015, **11**, 5940–5948.
26 C. Shenghai, S. Liping, K. Fanhao, H. Lihua and Z. Hui, *J. Power Sources*, 2019, **430**, 25–31.
27 Z. Wang, J. Ang, J. Liu, X. Y. D. Ma, J. Kong, Y. Zhang, T. Yan and X. Lu, *Appl. Catal., B*, 2020, **263**, 118344.
28 B. Zheng, Y. Zhou, C. Yu, S. Liu, Z. Pan, X. Wang, G. Liu and L. Lang, *J. Mater. Sci.*, 2020, **55**, 15454–15466.
29 M. Gong, W. Zhou, M. C. Tsai, J. Zhou, M. Guan, M. C. Lin, B. Zhang, Y. Hu, D. Y. Wang, J. Yang, S. J. Pennycook, B. J. Hwang and H. Dai, *Nat. Commun.*, 2014, **5**, 1–6.
30 M. Ledendecker, G. Clavel, M. Antonietti and M. Shalom, *Adv. Funct. Mater.*, 2015, **25**, 393–399.
31 L. Trotochaud, S. L. Young, J. K. Ranney and S. W. Boettcher, *J. Am. Chem. Soc.*, 2014, **136**, 6744–6753.
32 I. Aziz, J. G. Lee, H. Duran, K. Kirchhoff, R. T. Baker, J. T. S. Irvine and S. N. Arshad, *RSC Adv.*, 2019, **9**, 36586–36599.
33 H. Liu, Y. Zhang, R. Li, X. Sun, S. Désilets, H. Abou-Rachid, M. Jaidann and L. S. Lussier, *Carbon*, 2010, **48**, 1498–1507.
34 W. Q. Deng, X. Xu and W. A. Goddard, *Nano Lett.*, 2004, **4**, 2331–2335.
35 X. Wang, Q. Li, H. Pan, Y. Lin, Y. Ke, H. Sheng, M. T. Swihart and G. Wu, *Nanoscale*, 2015, **7**, 20290–20298.
36 B. S. Murty, S. A. Kori and M. Chakraborty, *Int. Mater. Rev.*, 2002, **47**, 3–29.
37 E. A. Holm and S. M. Foiles, *Science*, 2010, **328**, 1138–1141.
38 H. bin Wu, B. Y. Xia, L. Yu, X. Y. Yu and X. W. Lou, *Nat. Commun.*, 2015, **6**, 1–8.
39 J.-I. Jung, M. Risch, S. Park, M. G. Kim, G. Nam, H.-Y. Jeong, Y. Shao-Horn and J. Cho, *Energy Environ. Sci.*, 2016, **9**, 176–183.
40 Q. Wang, L. Shang, R. Shi, X. Zhang, Y. Zhao, G. I. N. Waterhouse, L. Z. Wu, C. H. Tung and T. Zhang, *Adv. Energy Mater.*, 2017, **7**, 1–7.
41 X. Zheng, Y. Zhang, H. Liu, D. Fu, J. Chen, J. Wang, C. Zhong, Y. Deng, X. Han and W. Hu, *Small*, 2018, **14**, 1–10.
42 Z. Wang, J. Ang, J. Liu, X. Y. D. Ma, J. Kong, Y. Zhang, T. Yan and X. Lu, *Appl. Catal., B*, 2020, **263**, 118344.
43 Y. Meng, J. C. Li, S. Y. Zhao, C. Shi, X. Q. Li, L. Zhang, P. X. Hou, C. Liu and H. M. Cheng, *Appl. Catal., B*, 2021, **294**, 120239.
44 C. S. Lim, C. K. Chua, Z. Sofer, K. Klímová, C. Boothroyd and M. Pumera, *J. Mater. Chem. A*, 2015, **3**, 11920–11929.
45 G. Wu, A. Santandreu, W. Kellogg, S. Gupta, O. Ogoke, H. Zhang, H. L. Wang and L. Dai, *Nano Energy*, 2016, **29**, 83–110.
46 G. Wu and P. Zelenay, *Acc. Chem. Res.*, 2013, **46**, 1878–1889.
47 Y. Yan, J. Miao, Z. Yang, F. X. Xiao, H. bin Yang, B. Liu and Y. Yang, *Chem. Soc. Rev.*, 2015, **44**, 3295–3346.